

Enhancing Out-of-Distribution Detection in Medical Imaging with Normalizing Flows

Dariush Lotfi¹, Mohammad-Ali Nikouei Mahani¹, Mohamad Koohi-Moghadam^{1*}, Kyongtae Ty Bae^{1*}

¹ Department of Diagnostic Radiology, Li Ka Shing Faculty of Medicine, The University of Hong Kong, Pok Fu Lam, Hong Kong

* Corresponding authors: KTB (baekt@hku.hk), MK (koohi@hku.hk)

Abstract

Purpose:

Out-of-distribution (OOD) detection is critical in AI-driven medical imaging to identify inputs that deviate from a model’s training distribution, ensuring reliability and safety in clinical workflows. Existing OOD detection methods often require modifications to pre-trained models or retraining, which is impractical in clinical settings. This study introduces a post-hoc normalizing flow-based approach for OOD detection, designed for seamless integration with pre-trained models.

Materials and Methods:

Our method leverages normalizing flows, a class of probabilistic generative models, to estimate the likelihood of feature vectors extracted from pre-trained models. Unlike traditional methods, it operates in feature space to capture semantically meaningful representations, avoiding reliance on pixel-level statistics. We evaluated our approach using the MedMNIST benchmark and a newly curated MedOOD dataset, simulating clinically relevant distributional shifts. Performance was assessed using standard OOD detection metrics, including AUROC, FPR@95, AUPR_IN, and AUPR_OUT. Statistical analyses, including DeLong's test and bootstrapping, were conducted to compare our method against ten baseline approaches.

Results:

On MedMNIST, our model achieved an AUROC of 93.80%, outperforming state-of-the-art methods such as ViM (88.08%) and ReAct (87.05%) ($P < 0.001$). It excelled across near and far OOD categories, achieving perfect scores in far OOD detection. On MedOOD, it achieved an AUROC of 84.61%, with significant improvements in handling transformation, modality, and organ shifts.

Conclusion:

Our normalizing flow-based method demonstrated superior performance in OOD detection while preserving ID accuracy. Its post-hoc nature enables direct integration with pre-trained models in clinical workflows. The model and code to build OOD datasets are available at <https://github.com/dlotfi/MedOODFlow>.

Summary:

A robust post-hoc OOD detection method for AI-driven medical imaging that ensures reliable and safe identification of distributional shifts without modifying pre-trained models.

Key Points

- The proposed normalizing flow-based model provides a robust post-hoc OOD detection method utilizing features from a pre-trained model without requiring model retraining or modifications.
- We developed MedOOD, a new curated OOD benchmark dataset for medical imaging, designed to evaluate distributional shifts across transformation, modality, diagnostic, population, and organ variations. This dataset can serve as a benchmark for future research in OOD detection.
- The code to train our model and to build MedOOD datasets are publicly available at <https://github.com/dlotfi/MedOODFlow>.

Introduction

In recent years, artificial intelligence (AI) and deep learning techniques have been increasingly integrated into medical imaging workflows, offering enhanced diagnostic capabilities and improved efficiency (1). However, one critical challenge that persists in the deployment of AI models in medical imaging is the effective management of uncertainty (2). Accurately identifying and managing uncertain predictions is essential to ensure the reliability and safety of AI-assisted diagnostic processes, as any lapse can lead to significant diagnostic errors and adverse patient outcomes.

To address this, the detection and management of out-of-distribution (OOD) data become crucial. OOD data refers to inputs that differ substantially from the data distribution on which a model was trained (3). In the context of medical imaging, OOD data can arise due to variations in patient populations, imaging modalities, acquisition settings, or emerging pathological conditions not previously encountered by the AI model. When confronted with such data, AI models may produce unreliable or incorrect outputs, potentially leading to significant diagnostic errors and adverse patient outcomes (4). Therefore, the ability to accurately detect OOD instances is essential for ensuring the safety and effectiveness of AI-assisted medical imaging applications.

A variety of approaches have been proposed to address the OOD detection problem, ranging from post-hoc methods to training-time strategies. Early post-hoc approaches like Maximum Softmax Probability (MSP) (5) and ODIN (6) provided foundational methods by leveraging softmax probabilities and temperature scaling. However, these methods faced challenges such as overconfidence in OOD predictions. Energy-based OOD detection (7) addressed this issue by scoring samples using the logits' energy, offering better separation between in-distribution (ID) and OOD data. Building on this, SHE method (8) leverages modern Hopfield networks to memorize ID data patterns and computes energy scores based on alignment with these patterns, providing a novel perspective that enhances the distinction between ID and OOD samples. Additionally, ViM (9) introduces Virtual-logit Matching, which combines residual-based

features from the principal subspace with logits to create a virtual OOD logit, improving OOD detection performance across large-scale ImageNet benchmarks. Beyond logits, methods like MDS (10) evaluated OOD scores based on feature Mahalanobis distances, emphasizing the role of intermediate representations. Similarly, the Gram method (11) characterizes feature correlations at multiple layers through Gram matrices and their higher-order extensions, identifying anomalies in activity patterns by comparing them to class-specific bounds observed during training.

Recent advancements have shifted toward activation shaping to improve OOD detection. ReAct (12) clipped high activations in the penultimate layer to reduce variance, while DICE (13) sparsified weights based on their contribution to outputs, achieving state-of-the-art results. ASH (14) introduced a two-step approach: pruning low-value activations and scaling the remaining ones, which significantly improved OOD detection performance. However, pruning in ASH can sometimes hinder performance. SCALE (15) refined this by focusing solely on scaling activations, achieving superior results without compromising ID accuracy. SCALE's use of sample-specific scaling factors enhances ID-OOD separability while preserving the logits' ordinality, making it highly effective across benchmarks.

Despite these advancements, existing approaches to OOD detection in medical imaging often face practical limitations. Many methods rely on modifying the training process, introducing additional regularization, or utilizing external datasets to improve model robustness. While effective, these strategies may be impractical in medical imaging settings, particularly when dealing with pre-trained models where retraining is infeasible due to computational constraints or regulatory considerations. To address these challenges, we propose a novel method for OOD detection using normalizing flows—a class of probabilistic generative models that enable likelihood estimation and efficient sampling (16). Unlike traditional methods that rely on pixel space density estimation, which often captures low-level statistics and spurious correlations (17, 18), our approach operates in the feature space of pre-trained models to focus on semantically meaningful representations. It operates in a post-hoc manner, allowing it to be applied to existing pre-trained models without modifying their weights or requiring retraining. Such a characteristic is particularly appealing in clinical scenarios where model retraining is impractical or where regulatory approvals have been granted for specific model configurations.

Materials and Methods

Model Architecture and Implementation

To detect OOD samples, we employed a normalizing flow-based model, inspired by the Real Non-Volume Preserving (RealNVP) model (19) (**Figure 1**). Normalizing flows are a class of generative models that enable exact computation of data likelihoods by transforming a simple probability distribution (e.g., a standard normal distribution) into a complex one that resembles the data distribution through a series of invertible and differentiable mappings (16). Since these transformations are invertible, normalizing flows can also transform data samples back to the standard normal distribution in latent space, while enabling efficient estimation of their probability density. One notable example is the RealNVP model, which maps input data \mathbf{x} into latent variables \mathbf{z} through a sequence of affine coupling layers. Each coupling layer applies a

transformation to a subset of the input variables conditioned on the remaining variables. Mathematically, the transformation in each coupling layer is defined as:

$$\begin{aligned} \mathbf{y}_{1:d} &= \mathbf{x}_{1:d}, \\ \mathbf{y}_{d+1:D} &= \mathbf{x}_{d+1:D} \odot \exp(s(\mathbf{x}_{1:d})) + t(\mathbf{x}_{1:d}), \end{aligned} \quad (1)$$

where $\mathbf{x} \in \mathbb{R}^D$ is the input feature vector, \mathbf{y} is the transformed output, d is the index dividing the input dimensions, $s(\cdot)$ and $t(\cdot)$ are scale and translation functions modeled by neural networks, and \odot denotes element-wise multiplication. This design ensures that the transformation is invertible and that the Jacobian determinant, required for likelihood computation, is easy to compute. Our model consisted of four masked affine coupling flows (19), each preceded by an ActNorm layer (20). The coupling network within each flow block consists of two multilayer perceptrons (MLPs) for the scale and translation functions. The MLPs had layer dimensions of [512, 1024, 512], enabling them to capture complex relationships in the feature space. The overall architecture allowed us to model the probability density function of the ID features extracted from the backbone network.

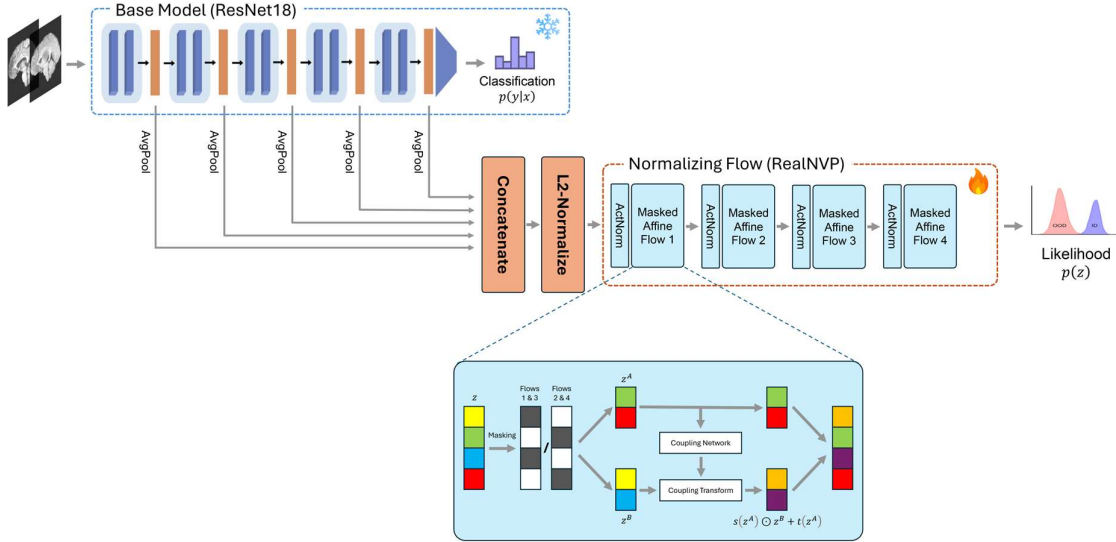


Figure 1: Architecture of the proposed model for OOD detection. Features extracted by the base/backbone model (ResNet18) are aggregated, L2-normalized, and passed to a normalizing flow with four masked affine coupling flows. The model estimates the probability density of ID features to compute likelihood scores for distinguishing ID and OOD samples.

The normalizing flow model was trained to maximize the log-likelihood of the ID feature vectors \mathbf{x} . The training objective is expressed as:

$$\mathcal{L} = -\frac{1}{N} \sum_{i=1}^N \log p_{\mathbf{x}}(\mathbf{x}^{(i)}) = -\frac{1}{N} \sum_{i=1}^N \log p_{\mathbf{z}}(\mathbf{z}^{(i)}) + \sum_{k=1}^K \log \left| \det \left(\frac{\partial f_k^{-1}(\mathbf{x}^{(i)})}{\partial \mathbf{x}} \right) \right| \quad (2)$$

where N is the number of training samples, $p_{\mathbf{x}}(\mathbf{x})$ is the density of the input data, $\mathbf{z}^{(i)} = f(\mathbf{x}^{(i)})$ is the transformed latent variable, $p_{\mathbf{z}}(\mathbf{z})$ is the base distribution (standard normal), K is the number of coupling layers, and f_k^{-1} denotes the inverse transformation at layer k . The term involving the determinant of the Jacobian accounts for the change of variables during transformation. We implemented our approach in PyTorch, building on the OpenOOD framework (21, 22). Details about the implementation, evaluation, and hyperparameters used to train the model are provided in **Supplementary Note 1**.

Benchmark and Curated Dataset

To rigorously evaluate our method, we utilized two types of datasets: a benchmark dataset (MedMNIST v2) (23) and a newly curated dataset by our team (MedOOD). MedMNIST v2, offered a diverse collection of standardized medical imaging datasets designed for machine learning research. These datasets allowed us to comprehensively assess ID and OOD performance across various imaging modalities and tasks. The curated MedOOD dataset was specifically constructed by us to simulate clinically relevant distributional shifts, providing an additional layer of evaluation to test the generalizability of our approach. This combination of datasets enabled a robust and thorough evaluation of our method under diverse and challenging conditions.

MedMNIST Benchmark Datasets

MedMNIST v2 covering a variety of medical imaging modalities such as X-ray, computed tomography (CT), dermoscopy, microscopy, fundus photography, and histopathology. The datasets are pre-processed into a uniform size of 28×28 pixels for 2D images, facilitating rapid experimentation while preserving essential diagnostic features. **Figure S1** shows a few samples of the datasets included in the MedMNIST benchmark.

We used OrganAMNIST (24) as ID dataset, which consists of axial CT images of abdominal organs labelled across 11 classes. We used OrganCMNIST (24), OrganSMNIST (24), ChestMNIST (25), PneumoniaMNIST (26) as near OOD datasets and PathMNIST (27), DermaMNIST (28), RetinaMNIST (29), and BloodMNIST (30) as far OOD datasets. This collection introduced significant variations in both anatomical regions and imaging modalities, providing a robust test for OOD detection. See **Table 1** for a detailed description of the MedMNIST 2D datasets, including their modalities and number of samples.

Table 1: Overview of MedMNIST benchmark datasets used in this study

Category	Dataset	Description	Number of Samples
In-Distribution (ID)	OrganAMNIST	Abdominal CT Axial view	58,850
Near OOD	OrganCMNIST	Abdominal CT Coronal view	8,268
	OrganSMNIST	Abdominal CT Sagittal view	8,829
	ChestMNIST	Chest X-ray	22,433
	PneumoniaMNIST	Chest X-ray	624
Far OOD	PathMNIST	Pathology	7,180
	DermaMNIST	Dermoscopy	2,005
	RetinaMNIST	Fundus Photography	400
	BloodMNIST	Blood Cell Microscopy	3,421

Note.—Of 58,850 OrganAMNIST samples, 41,072 were used to train the base classification model and normalizing flow model, while the remaining 17,778 were used to evaluate the OOD detection method.

MedOOD Curated Dataset

To further evaluate our method's generalizability, we curated a new OOD benchmark dataset, named MedOOD, from publicly available medical image repositories. This dataset includes images exhibiting various distributional shifts relevant to clinical practice. The curated ID dataset for this study comprises multi-center T1-weighted (T1w) brain MRIs of adult patients with glioma, primarily sourced from the BraTS 2020 (31-33) dataset (**Figure 2A**). The primary task involves binary classification of the whole volume into glioblastomas (GBM/HGG) and lower-grade gliomas (LGG). To further enhance the generalizability of the model, we used an additional in-domain dataset, LUMIERE (34), which consists of pre-operative T1w brain MRIs of glioblastoma patients acquired at the University Hospital of Bern, Switzerland. While LUMIERE shares the same imaging modality, organ, and pathology as the BraTS dataset, its data were obtained from a different imaging center, thereby simulating a realistic scenario where the model encounters unseen yet relevant ID data during deployment. The ID dataset is divided into three subsets: training, validation, and testing, consisting of 274, 20, and 155 samples, respectively. The testing subset comprises 75 samples from BraTS 2020 T1 and 80 samples from LUMIERE.

All brain imaging data underwent a preprocessing pipeline to ensure image de-identification and consistency with the BraTS data. De-facing was performed by skull-stripping the images using the HD-BET algorithm (35). The images were then registered to the SRI24 atlas (36) using ANTs (37), resampled to an isotropic voxel resolution of 1 mm³, standardized to an image size of 240×240×155 voxels, and normalized with intensity clipping at the upper and lower 0.1%. For non-brain datasets (abdominal and lumbar MRIs), resampling to 1 mm³, normalization, and center cropping were applied to match the target dimensions. For brain CT images, a window with a center of 40 and a width of 100 was applied to standardize intensity

levels. We followed (38, 39) to build the OOD samples and the detailed code of our implementation is available in our GitHub repository. Listed below are five categories of distributional shifts we used to build these OOD datasets. Additional details for each category are provided in **Supplementary Note 2**.

- **Transformation Shifts:** Simulated imaging artifacts and perturbations, including motion, ghosting, bias field inhomogeneity, RF pulse abnormalities, noise, downsampling, scaling, gamma alterations, truncation, and registration errors (75 OOD samples per transformation) (**Figure 2B**).
- **Population Shifts:** Assessed generalization using pediatric glioblastoma MRIs (99 scans) and Sub-Saharan African MRIs (60 scans), differing in age, quality, and disease presentation (**Figure 2C**).
- **Modality Shifts:** Evaluated cross-modality robustness using FLAIR and contrast-enhanced T1 (T1ce) MRIs (75 subjects) and pre-contrast CT scans (150 samples) (**Figure 2D**).
- **Diagnostic Shifts:** Included previously unseen pathologies: multiple sclerosis (170 scans), stroke (150 scans), epilepsy post-resection (150 scans), and healthy adults (150 scans) (**Figure 2E**).
- **Organ Shifts:** Evaluated extreme OOD cases using abdominal MRIs (80 scans) and lumbar spine MRIs (150 scans) (**Figure 2F**).

Evaluation and Statistical Analysis

We assessed the performance of our approach using four key metrics that are standard in OOD detection literature (21, 22): False Positive Rate at 95% True Positive Rate (FPR@95): This metric measures the proportion of ID samples incorrectly classified as OOD when the true positive rate (sensitivity) for OOD samples is set at 95%. A lower FPR@95 indicates better specificity, reducing the risk of unnecessary alerts in clinical settings. Area Under the Receiver Operating Characteristic Curve (AUROC): The AUROC provides a threshold-independent measure of the model's ability to distinguish between ID and OOD samples. Area Under the Precision-Recall Curve for In-Distribution Samples (AUPR_IN): This metric focuses on the model's precision and recall for ID samples, treating them as the positive class. High AUPR_IN values indicate that the model effectively identifies ID samples with a good balance of precision and recall, minimizing misclassification of ID samples as OOD. Area Under the Precision-Recall Curve for Out-of-Distribution Samples (AUPR_OUT): Conversely, AUPR_OUT evaluates the precision and recall for OOD samples as the positive class. High AUPR_OUT values reflect the model's effectiveness in detecting OOD samples with a good balance of precision and recall, reducing false negatives while maintaining high precision.

Statistical analyses were performed to compare our method against baseline post-hoc OOD detection approaches. The AUROC values were calculated, and 95% confidence intervals (CIs)

were estimated using the percentile bootstrap method with 1000 samples. Statistical significance for differences between AUROCs was assessed via bootstrapping, with a P -value threshold of 0.05 used to indicate significance. Paired comparisons were also conducted using the DeLong method.

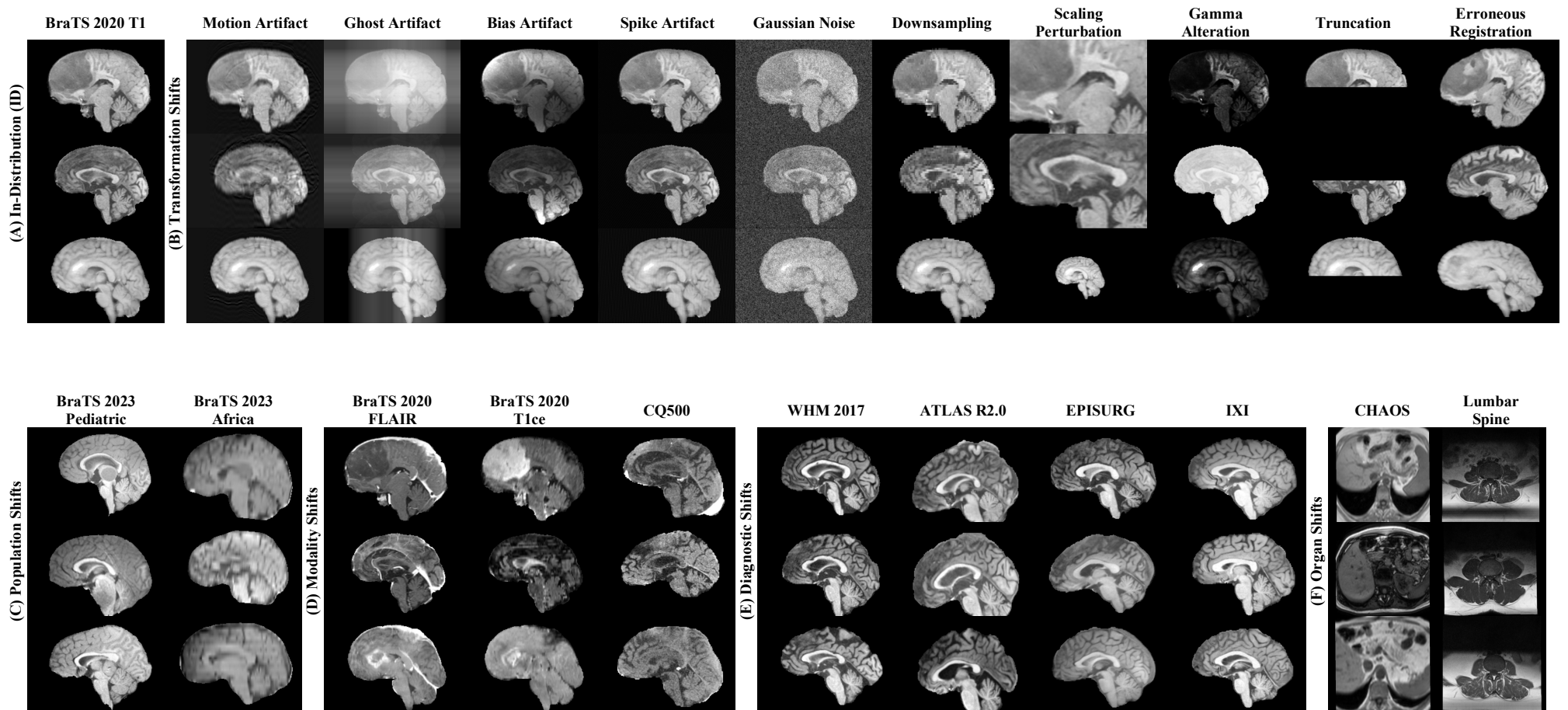


Figure 2: A few samples of the datasets included in MedOOD benchmark

Results

OOD detection on MedMNIST

The performance of our proposed method for OOD detection was evaluated on the MedMNIST dataset against ten publicly available post-hoc methods. Our method, utilizing features extracted from all five stages of the ResNet18 backbone, achieved the best performance across all metrics (**Table 2**), with an AUROC of 93.80%, significantly outperforming state-of-the-art methods such as ViM (9) (88.08%) and ReAct (12) (87.05%). For AUPR_IN, which measures the model's precision and recall for ID samples, our method achieved the highest value (84.17%), surpassing ViM (73.64%) and ReAct (73.00%). For AUPR_OUT, our method also excelled with a value of 97.90%, indicating a high capacity to correctly identify OOD samples with minimal false negatives. Our model's improvement over the best baseline method, ViM, was statistically significant. The AUROC comparison between our model (93.80%) and ViM (88.08%) yielded a $P < 0.001$ using DeLong's test, indicating a significant improvement. Bootstrapping with 1000 iterations further confirmed statistical significance with a $P < 0.001$.

Table 2: Model performance comparison with other post-hoc methods on MedMNIST

Method	FPR@95 ↓	AUROC ↑	AUPR_IN ↑	AUPR_OUT ↑
MSP (2017) (5)	100 (44.1, 100)	85.5 (85.18, 85.85)	74.53 (74.03, 75.1)	92.85 (92.58, 93.11)
ODIN (2018) (6)	49.6 (48.25, 51.03)	86.67 (86.36, 87)	69.19 (68.44, 69.99)	93.70 (93.46, 93.93)
MDS (2018) (10)	80.37 (79.70, 81.02)	64.7 (64.20, 65.17)	42.74 (41.94, 43.48)	83.45 (83.08, 83.84)
Gram (2020) (11)	60.61 (59.79, 61.58)	78.54 (78.16, 78.93)	60.80 (60.06, 61.59)	90.71 (90.47, 90.94)
ReAct (2021) (12)	46.37 (45.11, 47.73)	87.05 (86.73, 87.39)	73.00 (72.33, 73.71)	93.68 (93.43, 93.92)
DICE (2022) (13)	76.74 (76.06, 77.43)	68.37 (67.96, 68.82)	46.03 (45.29, 46.81)	85.92 (85.58, 86.22)
ViM (2022) (9)	45 (43.71, 46.21)	88.08 (87.79, 88.39)	73.64 (72.98, 74.36)	94.40 (94.17, 94.61)
SHE (2023) (8)	59.4 (58.22, 60.59)	81.7 (81.32, 82.07)	62.74 (61.97, 63.55)	91.07 (90.77, 91.35)
ASH (2023) (14)	49.47 (47.90, 50.75)	86.6 (86.29, 86.96)	69.25 (68.53, 70.03)	93.55 (93.30, 93.79)
SCALE (2024) (15)	49.47 (47.90, 50.75)	86.6 (86.29, 86.96)	69.25 (68.53, 70.03)	93.55 (93.30, 93.79)
Ours (features of 5 stages)	36.3 (35.43, 37.19)	93.8 (93.63, 93.98)	84.17 (83.71, 84.6)	97.90 (97.83, 97.97)

Note.—All metrics were computed using micro-averaging, with 95% CIs in parentheses.

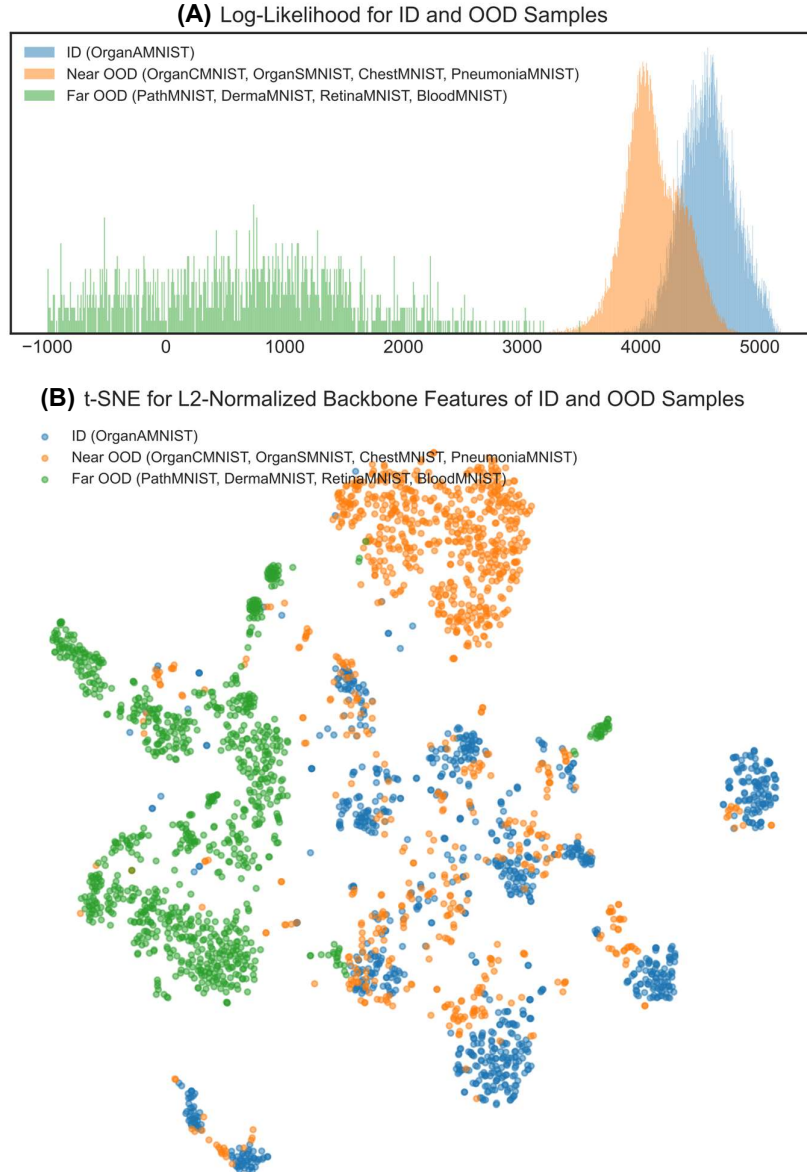


Figure 3: (A) Histogram of the log-likelihood values for ID features compared to near/far OOD features under the normalizing flow model. Better separability of these distributions shows better OOD detection. (B) t-SNE visualization of the feature space of a ResNet18 backbone model, illustrating ID vs near/far OOD features

Evaluation Across Near and Far OOD Categories in MedMNIST

To provide a more comprehensive evaluation of our proposed method, we assessed its performance on both near and far OOD categories within the MedMNIST dataset (**Table 3**). This finer-grained analysis highlights the robustness of our model across varying degrees of distributional shifts. For near OOD categories, which include datasets with distributions closer to the ID data, our model achieved an average AUROC of 90.21% and an average FPR@95 of

29.08%. The performance was particularly strong for datasets such as ChestMNIST (AUROC: 98.97%, FPR@95: 4.09%) and PneumoniaMNIST (AUROC: 97.87%, FPR@95: 6.54%), indicating the model's ability to effectively distinguish ID samples from OOD samples in scenarios where the shifts are subtle.

For far OOD categories, which represent datasets with distributions significantly different from the ID data, our model demonstrated exceptional performance, achieving perfect scores across all metrics. Specifically, for datasets such as PathMNIST, DermaMNIST, RetinaMNIST, and BloodMNIST, the model consistently achieved AUROC, AUPR_IN, and AUPR_OUT values of 100%, with FPR@95 reduced to 0. This indicates that the model can confidently and accurately detect OOD samples in cases of pronounced distributional shifts. To further analyze the performance of our method on near and far OOD categories, we utilized log-likelihood and t-SNE plots. The log-likelihood histogram (**Figure 3A**) shows clear separability between ID and OOD samples, with far-OOD samples exhibiting lower log-likelihood values and near-OOD samples positioned between ID and far-OOD distributions. The t-SNE visualization (**Figure 3B**) illustrates distinct clustering of ID and OOD samples in the feature space, reinforcing the effectiveness of our method in capturing meaningful semantic differences.

Table 3: Model performance on different categories and datasets of MedMNIST

Category	Dataset	FPR@95 ↓	AUROC ↑	AUPR_IN ↑	AUPR_OUT ↑
Near OOD	OrganCMNIST	61.43	78.19	89.21	61.45
	OrganSMNIST	44.24	85.79	92.9	73.38
	ChestMNIST	4.09	98.97	98.95	99.02
	PneumoniaMNIST	6.54	97.87	99.92	57.47
	Average	29.08	90.21	95.24	72.83
Far OOD	PathMNIST	0	100	100	100
	DermaMNIST	0	100	100	100
	RetinaMNIST	0	100	100	100
	BloodMNIST	0	100	100	100
	Average	0	100	100	100

OOD Detection on MedOOD Curated Dataset

The performance of our proposed method was further evaluated on the curated MedOOD dataset, using the same metrics and comparison framework as in the MedMNIST evaluation. The results were computed using micro-averaging, with an input size of 112×112×112. As Shown in **Table 4**, our method when using features extracted from all five stages of the 3D-ResNet18 backbone, achieved an AUROC of 84.61%, outperforming state-of-the-art methods such as ViM (9) (80.65%) and MDS (10) (80.87%). For FPR@95, our model achieved a value of 67.74%, showing better specificity compared to ViM (76.77%) and MDS (76.13%).

The improvement in AUROC achieved by our model over ViM (AUROC 80.65%, 95% CI: 78.24–83.11) was statistically significant, as confirmed by DeLong’s test ($P = 0.0105$) and bootstrapping with 1000 iterations ($P = 0.006$). Similarly, our model outperformed MDS (AUROC 80.87%, 95% CI: 78.30–83.63), with statistical significance validated using DeLong’s test ($P = 0.0126$) and bootstrapping with 1000 iterations ($P = 0.01$).

Table 4: Model performance comparison with other post-hoc methods on MedOOD

Method	FPR@95 ↓	AUROC ↑	AUPR_IN ↑	AUPR_OUT ↑
MSP (2017) (5)	100 (100, 100)	46.57 (42.42, 50.31)	5.99 (5.02, 7.06)	92.92 (91.42, 94.21)
ODIN (2018) (6)	100 (100, 100)	46.6 (42.5, 50.36)	5.99 (5.02, 7.05)	93.02 (91.54, 94.31)
MDS (2018) (10)	76.13 (69.13, 83.52)	80.87 (78.3, 83.63)	21.58 (17.07, 27.63)	98.33 (97.96, 98.68)
Gram (2020) (11)	100 (100, 100)	29.51 (26.73, 32.22)	4.64 (3.95, 5.38)	90.50 (88.83, 91.85)
ReAct (2021) (12)	100 (100, 100)	46.85 (42.99, 50.59)	6.03 (5.03, 7.10)	93.40 (92.04, 94.49)
DICE (2022) (13)	100 (100, 100)	41.85 (38.91, 44.77)	5.55 (4.69, 6.44)	93.20 (91.91, 94.28)
ViM (2022) (9)	76.77 (68.25, 84.07)	80.65 (78.24, 83.11)	21.12 (16.54, 27.15)	98.30 (97.93, 98.67)
SHE (2023) (8)	100 (100, 100)	38.15 (35.08, 41)	5.23 (4.4, 6.06)	92.42 (91.03, 93.6)
ASH (2023) (14)	100 (100, 100)	50.04 (46.35, 53.43)	6.37 (5.34, 7.5)	94.24 (93.07, 95.19)
SCALE (2024) (15)	100 (100, 100)	50.04 (46.35, 53.43)	6.37 (5.34, 7.5)	94.24 (93.07, 95.19)
Ours (features of 5 stages)	67.74 (58.45, 74.86)	84.61 (82.12, 87.16)	31.36 (24.76, 38.47)	98.64 (98.32, 98.97)

Note.—All metrics were computed using micro-averaging, with 95% CIs in parentheses.

OOD Detection Across Diverse Shifts in MedOOD

To further validate the robustness of our proposed method, we conducted a detailed analysis on the curated MedOOD dataset by evaluating its performance across different subcategories, including transformation shifts, population shifts, modality shifts, diagnostic shifts, and organ shifts (**Table 5**). For transformation shifts, our model achieved an average AUROC of 91.01% and FPR@95 of 24.39%, with perfect performance (AUROC: 100%, FPR@95: 0) on Motion, Ghost, Spike, and Noise datasets. However, it faced challenges with Downsampling (AUROC: 61.56%, FPR@95: 90.32%) and Gamma shifts (AUROC: 78.19%, FPR@95: 67.74%). For population shifts, the average AUROC was 70.34%, with better performance on BraTS 2023

Pediatric (AUROC: 80.53%) compared to BraTS 2023 Africa (AUROC: 60.14%). These shifts proved more challenging, reflected in lower AUPR_OUT (54.57%). For modality shifts, the model showed strong generalization (AUROC: 94.40%, FPR@95: 22.58%), excelling on CQ500 (AUROC: 99.06%) and BraTS 2020 T1ce (AUROC: 96.36%). For diagnostic shifts, performance was more variable, with an average AUROC of 68.36%. WHM 2017 performed best (AUROC: 84.55%), while ATLAS R2.0 posed challenges (AUROC: 58.96%). For organ shifts, the model achieved perfect scores (AUROC: 100%, FPR@95: 0), demonstrating exceptional robustness to anatomical variations.

Table 5. Model performance on different categories and datasets of MedOOD

Category	Dataset	FPR@95 ↓	AUROC ↑	AUPR_IN ↑	AUPR_OUT ↑
Transformation Shifts	Motion Artifact	0	100	100	100
	Ghost Artifact	0	100	100	100
	Bias Artifact	17.42	96.22	98.26	91.9
	Spike Artifact	0	100	100	100
	Gaussian Noise	0	100	100	100
	Downsampling	90.32	61.56	76.8	40.89
	Scaling Perturbation	0	100	100	100
	Gamma Alteration	67.74	78.19	88.07	62.72
	Truncation	0.65	99.85	99.93	99.68
	Erroneous Registration	67.74	74.29	84.61	54.81
	Average	24.39	91.01	94.77	85
Population Shifts	BraTS 2023 Pediatric	71.61	80.53	87.11	69.56
	BraTS 2023 Africa	85.16	60.14	79.28	39.58
	Average	78.39	70.34	83.2	54.57
Modality Shifts	BraTS 2020 FLAIR	48.39	87.78	93.94	72.84
	BraTS 2020 T1ce	15.48	96.36	98.32	93.01
	CQ500	3.87	99.06	99.31	98.74
	Average	22.58	94.4	97.19	88.2
Diagnostic Shifts	IXI	83.87	62.69	66.06	56.15
	WHM 2017	54.19	84.55	85.66	77.28
	EPISURG	72.26	67.23	70.83	59.49
	ATLAS R2.0	82.58	58.96	65.57	51.81
	Average	73.23	68.36	72.03	61.18
Organ Shifts	CHAOS	0	100	100	100
	Lumbar Spine	0	100	100	100
	Average	0	100	100	100

Besides, we conducted a comparison of AUROC scores between our method and ViM across all these subcategories (**Figure 4**). Our method consistently outperformed ViM in transformation shifts and diagnostic shifts, with significant improvements on challenging datasets such as Downsampling, Gamma Alteration, Erroneous Registration, WMH 2017, and IXI. It also performed comparably to ViM in modality shifts and showed exceptional robustness in organ shifts, achieving perfect scores on CHAOS and Lumbar Spine datasets. However, challenges remain in specific population shifts, such as BraTS 2023 Africa, and certain diagnostic datasets, like ATLAS R2.0. Overall, when evaluated across all data, our method demonstrated better performance compared to ViM. A details of ablation study can be found in **Supplementary Note 3**.

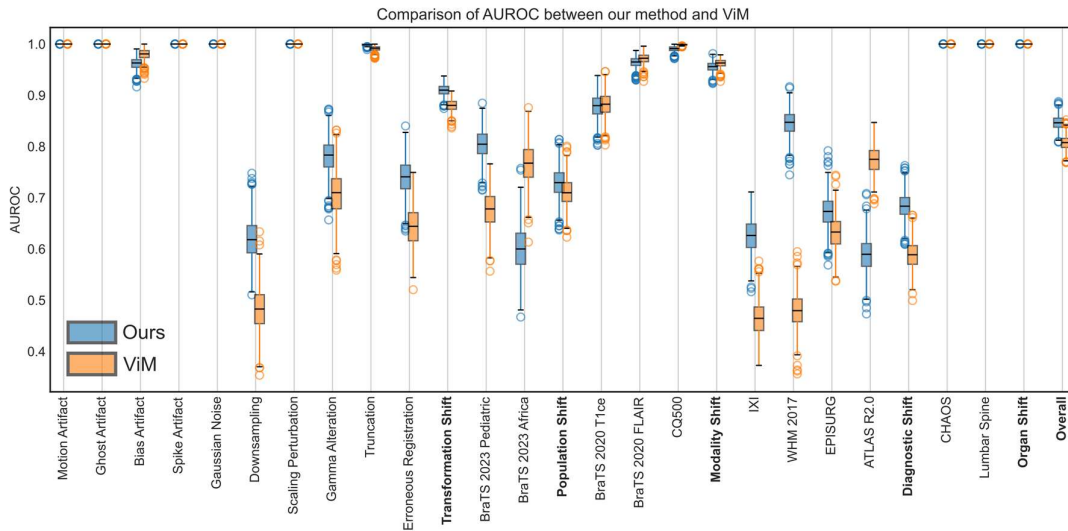


Figure 4: Model performance comparison with ViM on different categories and datasets of MedOOD

Discussion

The integration of AI into medical imaging necessitates robust methods to identify OOD data, as diagnostic errors from undetected distributional shifts can have critical clinical consequences. Our study introduces a post-hoc normalizing flow-based approach that addresses this challenge without requiring modifications to pre-trained models, enabling seamless deployment in clinical workflows. The results demonstrate significant advancements over existing methods, highlighting both the technical efficacy and practical utility of our method.

Our proposed method demonstrated superior performance compared to state-of-the-art post-hoc OOD detection approaches, including ViM and ReAct, across diverse datasets and evaluation metrics. By leveraging normalizing flows, which enable exact likelihood estimation and efficient sampling, the method captures complex underlying data distributions more effectively than existing techniques. This capability is particularly valuable in safety-critical medical imaging applications, where accurate OOD detection is essential to mitigate risks associated with diagnostic errors and improve clinical decision-making.

The evaluation on the curated MedOOD dataset further underscores the generalizability of our approach. The method achieved exceptional performance in detecting a wide range of OOD scenarios, including transformation, modality, and organ shifts. Perfect scores on organ shifts and specific transformation shifts (e.g., motion artifact, ghost artifact, and Gaussian noise) highlight the robustness of the model in handling extreme or unexpected cases that may arise during clinical deployment. By detecting these shifts with high precision, the method can act as a safeguard, ensuring that models flag unfamiliar inputs for further review rather than producing unreliable outputs.

Another significant advantage of our approach is its post-hoc nature, which enables direct integration into pre-existing medical imaging workflows. Retraining AI models in clinical settings can be time-consuming, computationally expensive, and subject to regulatory constraints. Our method circumvents these challenges by operating independently of the original training process, offering immediate improvements in safety and reliability without requiring modifications to already-approved models. This characteristic is especially important for models deployed in diverse clinical environments, where variability in equipment, acquisition protocols, and patient demographics is common.

While our proposed method demonstrates strong performance across diverse datasets and scenarios, certain limitations should be acknowledged. The model showed lowered performance in handling subtle population shifts, such as demographic variations in the MedOOD dataset, indicating potential challenges in generalizing to less apparent distributional changes. Similarly, while the method performed well on many diagnostic shifts, its variability across certain datasets suggests room for improvement in capturing nuanced differences associated with unseen pathologies. These findings highlight the need for further refinement to address under-represented populations and clinical conditions, which are critical for ensuring the equity and reliability of AI systems in diverse healthcare settings. To address these limitations and further improve the efficacy of our method, future research could focus on enhancing the model's robustness to subtle population and diagnostic shifts.

Author contributions: Guarantors of integrity of entire study, D. L., M. K., K. T. B; study concepts/study design or data acquisition or data analysis/interpretation, all authors; manuscript drafting or manuscript revision for important intellectual content, all authors; approval of final version of submitted manuscript, all authors; agrees to ensure any questions related to the work are appropriately resolved, all authors; literature research, D. L., M. K., K. T. B; model development and evaluation, D. L.; and manuscript editing, D. L., M. K., K. T. B.

Disclosures of conflicts of interest: The authors declare no competing financial or non-financial interests.

Data availability

The code and database are publicly accessible at <https://github.com/dlotfi/MedOODFlow>.

References

1. Rajpurkar P, Chen E, Banerjee O, Topol EJ. AI in health and medicine. *Nature medicine*. 2022;28(1):31-8.
2. Huang L, Ruan S, Xing Y, Feng M. A review of uncertainty quantification in medical image analysis: probabilistic and non-probabilistic methods. *Medical Image Analysis*. 2024:103223.
3. Zhang O, Delbrouck J-B, Rubin DL, editors. Out of distribution detection for medical images. *Uncertainty for Safe Utilization of Machine Learning in Medical Imaging, and Perinatal Imaging, Placental and Preterm Image Analysis: 3rd International Workshop, UNSURE 2021, and 6th International Workshop, PIPPI 2021, Held in Conjunction with MICCAI 2021, Strasbourg, France, October 1, 2021, Proceedings 3*; 2021: Springer.
4. Yang Y, Zhang H, Gichoya JW, Katabi D, Ghassemi M. The limits of fair medical imaging AI in real-world generalization. *Nature Medicine*. 2024;30(10):2838-48.
5. Hendrycks D, Gimpel K, editors. A Baseline for Detecting Misclassified and Out-of-Distribution Examples in Neural Networks. *International Conference on Learning Representations*; 2017.
6. Liang S, Li Y, Srikant R, editors. Enhancing The Reliability of Out-of-distribution Image Detection in Neural Networks. *International Conference on Learning Representations*; 2018.
7. Liu W, Wang X, Owens JD, Li Y. Energy-based Out-of-distribution Detection. *Advances in Neural Information Processing Systems*. 2020;33:21464-75.
8. Zhang J, Fu Q, Chen X, Du L, Li Z, Wang G, et al., editors. Out-of-Distribution Detection based on In-Distribution Data Patterns Memorization with Modern Hopfield Energy. *The Eleventh International Conference on Learning Representations*; 2023.
9. Wang H, Li Z, Feng L, Zhang W. ViM: Out-Of-Distribution with Virtual-logit Matching. *Proceedings of the IEEE Computer Society Conference on Computer Vision and Pattern Recognition*. 2022;2022-June:4911-20.
10. Lee K, Lee K, Lee H, Shin J, editors. A Simple Unified Framework for Detecting Out-of-Distribution Samples and Adversarial Attacks. *Advances in Neural Information Processing Systems*; 2018: Curran Associates, Inc.
11. Sastry CS, Oore S, editors. Detecting Out-of-Distribution Examples with Gram Matrices. *Proceedings of the 37th International Conference on Machine Learning*; 2020 2020/1//: PMLR.
12. Sun Y, Guo C, Li Y, editors. ReAct: Out-of-distribution Detection With Rectified Activations. *Advances in Neural Information Processing Systems*; 2021: Curran Associates, Inc.
13. Sun Y, Li Y, editors. DICE: Leveraging Sparsification for Out-of-Distribution Detection. *Computer Vision – ECCV 2022*; 2022; Cham: Springer Nature Switzerland.
14. Djuricic A, Bozanic N, Ashok A, Liu R, editors. Extremely Simple Activation Shaping for Out-of-Distribution Detection. *The Eleventh International Conference on Learning Representations*; 2023.
15. Xu K, Chen R, Franchi G, Yao A, editors. Scaling for Training Time and Post-hoc Out-of-distribution Detection Enhancement. *The Twelfth International Conference on Learning Representations*; 2024.

16. Rezende D, Mohamed S, editors. Variational Inference with Normalizing Flows. Proceedings of the 32nd International Conference on Machine Learning; 2015 2015/1//; Lille, France: PMLR.
17. Kirichenko P, Izmailov P, Wilson AG, editors. Why Normalizing Flows Fail to Detect Out-of-Distribution Data. Advances in Neural Information Processing Systems; 2020: Curran Associates, Inc.
18. Nalisnick E, Matsukawa A, Teh YW, Gorur D, Lakshminarayanan B, editors. Do Deep Generative Models Know What They Don't Know? International Conference on Learning Representations; 2019.
19. Dinh L, Sohl-Dickstein J, Bengio S, editors. Density estimation using Real NVP. International Conference on Learning Representations; 2017.
20. Kingma DP, Dhariwal P, editors. Glow: Generative Flow with Invertible 1x1 Convolutions. Advances in Neural Information Processing Systems; 2018: Curran Associates, Inc.
21. Yang J, Wang P, Zou D, Zhou Z, Ding K, Peng W, et al., editors. OpenOOD: benchmarking generalized out-of-distribution detection. Proceedings of the 36th International Conference on Neural Information Processing Systems; 2024; Red Hook, NY, USA: Curran Associates Inc.
22. Zhang J, Yang J, Wang P, Wang H, Lin Y, Zhang H, et al. OpenOOD v1.5: Enhanced Benchmark for Out-of-Distribution Detection. Journal of Data-centric Machine Learning Research. 2023.
23. Yang J, Shi R, Wei D, Liu Z, Zhao L, Ke B, et al. MedMNIST v2 - A large-scale lightweight benchmark for 2D and 3D biomedical image classification. Scientific Data 2023 10:1. 2023;10(1):1-10.
24. Xu X, Zhou F, Liu B, Fu D, Bai X. Efficient Multiple Organ Localization in CT Image Using 3D Region Proposal Network. IEEE Transactions on Medical Imaging. 2019;38(8):1885-98.
25. Wang X, Peng Y, Lu L, Lu Z, Bagheri M, Summers RM. ChestX-Ray8: Hospital-Scale Chest X-Ray Database and Benchmarks on Weakly-Supervised Classification and Localization of Common Thorax Diseases. 2017 IEEE Conference on Computer Vision and Pattern Recognition (CVPR). 2017;2017-January:3462-71.
26. Kermany DS, Goldbaum M, Cai W, Valentim CCS, Liang H, Baxter SL, et al. Identifying Medical Diagnoses and Treatable Diseases by Image-Based Deep Learning. Cell. 2018;172(5):1122-31.e9.
27. Kather JN, Krisam J, Charoentong P, Luedde T, Herpel E, Weis CA, et al. Predicting survival from colorectal cancer histology slides using deep learning: A retrospective multicenter study. PLOS Medicine. 2019;16(1):e1002730-e.
28. Tschandl P, Rosendahl C, Kittler H. The HAM10000 dataset, a large collection of multi-source dermatoscopic images of common pigmented skin lesions. Scientific Data 2018 5:1. 2018;5(1):1-9.
29. Liu R, Wang X, Wu Q, Dai L, Fang X, Yan T, et al. DeepDRiD: Diabetic Retinopathy—Grading and Image Quality Estimation Challenge. Patterns. 2022;3(6):100512-.
30. Acevedo A, Merino A, Alférez S, Molina Á, Boldú L, Rodellar J. A dataset of microscopic peripheral blood cell images for development of automatic recognition systems. Data in Brief. 2020;30:105474-.

31. Bakas S, Akbari H, Sotiras A, Bilello M, Rozycki M, Kirby JS, et al. Advancing The Cancer Genome Atlas glioma MRI collections with expert segmentation labels and radiomic features. *Scientific data*. 2017;4.
32. Menze BH, Jakab A, Bauer S, Kalpathy-Cramer J, Farahani K, Kirby J, et al. The Multimodal Brain Tumor Image Segmentation Benchmark (BRATS). *IEEE transactions on medical imaging*. 2015;34(10):1993-2024.
33. Bakas S, Reyes M, Jakab A, Bauer S, Rempfler M, Crimi A, et al. Identifying the Best Machine Learning Algorithms for Brain Tumor Segmentation, Progression Assessment, and Overall Survival Prediction in the BRATS Challenge. *Sandra Gonzlez-Vill*. 2018;124.
34. Suter Y, Knecht U, Valenzuela W, Notter M, Hewer E, Schucht P, et al. The LUMIERE dataset: Longitudinal Glioblastoma MRI with expert RANO evaluation. *Scientific Data*. 2022;9(1).
35. Isensee F, Schell M, Pflueger I, Brugnara G, Bonekamp D, Neuberger U, et al. Automated brain extraction of multisequence MRI using artificial neural networks. *Human Brain Mapping*. 2019;40(17):4952-64.
36. Rohlfing T, Zahr NM, Sullivan EV, Pfefferbaum A. The SRI24 multichannel atlas of normal adult human brain structure. *Human Brain Mapping*. 2010;31(5):798-819.
37. Tustison NJ, Cook PA, Holbrook AJ, Johnson HJ, Muschelli J, Devenyi GA, et al. The ANTsX ecosystem for quantitative biological and medical imaging. *Scientific Reports*. 2021;11(1):9068-.
38. Lambert B. Quantifying and understanding uncertainty in deep-learning-based medical image segmentation. *Université Grenoble Alpes [2020-....]*; 2024.
39. Lambert B, Forbes F, Doyle S, Dojat M. Multi-layer Aggregation as a Key to Feature-Based OOD Detection. 2023:104-14.
40. Kingma DP, Ba J. Adam: A Method for Stochastic Optimization. *CoRR*. 2014;abs/1412.6980.
41. Al-Dhabyani W, Gomaa M, Khaled H, Fahmy A. Dataset of breast ultrasound images. *Data in Brief*. 2020;28:104863-.
42. He K, Zhang X, Ren S, Sun J. Deep residual learning for image recognition. *Proceedings of the IEEE Computer Society Conference on Computer Vision and Pattern Recognition*. 2016;2016-December:770-8.
43. Hara K, Kataoka H, Satoh Y. Can Spatiotemporal 3D CNNs Retrace the History of 2D CNNs and ImageNet? *Proceedings of the IEEE Computer Society Conference on Computer Vision and Pattern Recognition*. 2018:6546-55.
44. Kazerooni AF, Khalili N, Liu X, Haldar D, Jiang Z, Anwar SM, et al. The Brain Tumor Segmentation (BraTS) Challenge 2023: Focus on Pediatrics (CBTN-CONNECT-DIPGR-ASNR-MICCAI BraTS-PEDs). *ArXiv*. 2023:arXiv:2305.17033v7-arXiv:2305.v7.
45. Adewole M, Rudie JD, Gbadamosi A, Toyobo O, Raymond C, Zhang D, et al. The Brain Tumor Segmentation (BraTS) Challenge 2023: Glioma Segmentation in Sub-Saharan Africa Patient Population (BraTS-Africa). *ArXiv*. 2023:arXiv:2305.19369v1-arXiv:2305.v1.
46. Chilamkurthy S, Ghosh R, Tanamala S, Biviji M, Campeau NG, Kumar Venugopal V, et al. Development and Validation of Deep Learning Algorithms for Detection of Critical Findings in Head CT Scans. 2018.
47. Kuijf HJ, Casamitjana A, Collins DL, Dadar M, Georgiou A, Ghafoorian M, et al. Standardized Assessment of Automatic Segmentation of White Matter Hyperintensities and

Results of the WMH Segmentation Challenge. IEEE Transactions on Medical Imaging. 2019;38(11):2556-68.

48. Liew SL, Lo BP, Donnelly MR, Zavaliangos-Petropulu A, Jeong JN, Barisano G, et al. A large, curated, open-source stroke neuroimaging dataset to improve lesion segmentation algorithms. Scientific Data 2022 9:1. 2022;9(1):1-12.

49. Pérez-García F, Rodionov R, Alim-Marvasti A, Sparks R, Duncan JS, Ourselin S. Simulation of Brain Resection for Cavity Segmentation Using Self-supervised and Semi-supervised Learning. Lecture Notes in Computer Science (including subseries Lecture Notes in Artificial Intelligence and Lecture Notes in Bioinformatics). 2020;12263 LNCS:115-25.

50. IXI Dataset – Brain Development Available from: <https://brain-development.org/ixi-dataset/>.

51. Kavur AE, Gezer NS, Barış M, Aslan S, Conze PH, Groza V, et al. CHAOS Challenge - combined (CT-MR) healthy abdominal organ segmentation. Medical Image Analysis. 2021;69:101950-.

52. Natalia F, Meidia H, Afriliana N, Al-Kafri AS, Sudirman S, Simpson A, et al. Development of Ground Truth Data for Automatic Lumbar Spine MRI Image Segmentation. Proceedings - 20th International Conference on High Performance Computing and Communications, 16th International Conference on Smart City and 4th International Conference on Data Science and Systems, HPCC/SmartCity/DSS 2018. 2019:1449-54.

Supplementary Information

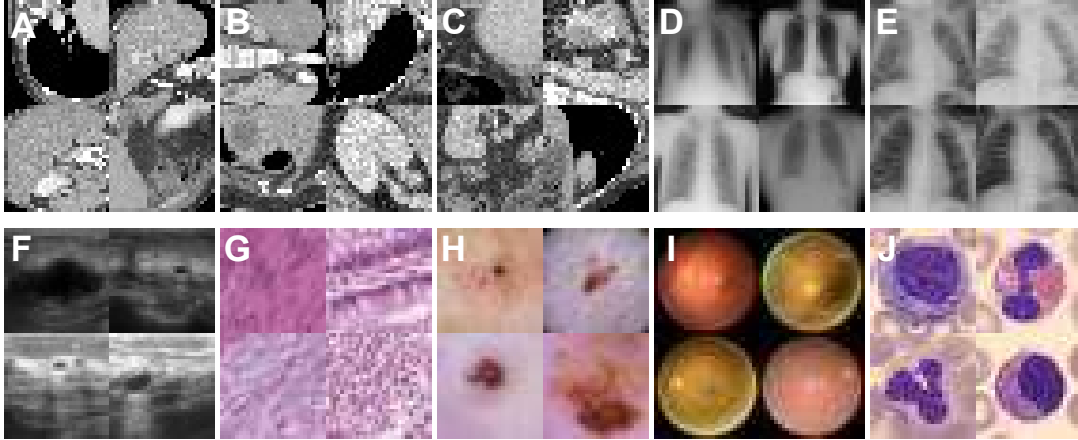


Figure S1: A few samples of the datasets included in MedMNIST benchmark. (A) OrganAMNIST (B) OrganCMNIST (C) OrganSMNIST (D) ChestMNIST (E) PneumoniaMNIST (F) BreastMNIST (G) PathMNIST (H) DermaMNIST (I) RetinaMNIST (J) BloodMNIST

Table S1: Overview of MedOOD benchmark datasets used in this study

Category	Dataset	Description	Number of Samples
In-Distribution (ID)	BraTS 2020 T1w	Multi-center T1w brain MRIs of adults with glioma	369
	LUMIERE	Pre-operative T1w MRIs of adults with gliomas from a different imaging center, simulating unseen clinical data	80
Transformation Shifts	Motion Artifact	Simulating head movements during acquisition	75
	Ghost Artifact	Mimicking periodic motion artifacts	75
	Bias Artifact	Replicating non-uniform illumination caused by magnetic field inhomogeneity	75
	Spike Artifact	Emulating Herringbone artifacts caused by aberrant k-space points	75
	Gaussian Noise	Adding random noise ($\mu = 0, \sigma = 0.5$) to normalized images	75
	Downsampling	Simulating low-resolution images	75
	Scaling Perturbation	Altering brain size (halving or doubling)	75

	Gamma Alteration	Simulating extreme contrast changes	75
	Truncation	Mimicking missing data or file transfer errors	75
	Erroneous Registration	Simulating errors during registration	75
Population Shifts	BraTS 2023 Pediatric	T1w MRIs of children with glioblastoma	99
	BraTS 2023 Africa	MRIs from adult patients in Sub-Saharan Africa	60
Modality Shifts	BraTS 2020 FLAIR	Corresponding FLAIR sequences of the test ID subjects from BraTS 2020	75
	BraTS 2020 T1ce	Corresponding contrast-enhanced T1 (T1ce) sequences of the test ID subjects from BraTS 2020	75
	CQ500	Pre-contrast brain CT scans	150
Diagnostic Shifts	WHM 2017	T1w MRIs of patients with multiple sclerosis	150
	ATLAS R2.0	T1w MRIs of patients having brain stroke	150
	EPISURG	T1w MRIs from patients who underwent brain resection for epilepsy treatment	150
	IXI	T1w MRIs of healthy young adults	150
Organ Shifts	CHAOS	T1w abdominal MRIs	80
	Lumbar Spine	Lumbar spine T1w MRIs	150

Note.—Of 369 T1w MRI volumes in BraTS 2020, 294 were used to train the base classification model and normalizing flow model, while the remaining 75 were used to evaluate the OOD detection method. We have included the code and instructions in our GitHub repository for constructing this dataset: <https://github.com/dlotfi/MedOODFlow/blob/main/medood/README.md>

Supplementary Note 1:

Model implementation and evaluation details: Training was conducted using the Adam optimizer (40) over 100 epochs with a learning rate of 1×10^{-4} . The model parameters were initialized randomly. Importantly, the training was unsupervised with respect to OOD data, and we only used the ID data for training our model. This approach eliminates the need for OOD examples during training, reducing potential biases and ensuring the method remains generalizable. Model selection was performed using the Area Under the Receiver Operating Characteristic Curve (AUROC) as the evaluation metric. During training, we assessed the model's ability to distinguish between ID samples from the OrganAMNIST (24) validation set and OOD samples from the BreastMNIST (41) validation set. The model with the highest AUROC on this validation criterion was selected for further evaluation. To ensure consistency and comparability across experiments, we applied the same approach to train a normalizing flow model for our curated MedOOD dataset. For MedOOD, the BraTS 2020 T1 and T2 (32) validation sets were used as ID and OOD to select the best-performing normalizing flow model. We implemented our approach in PyTorch, building on the OpenOOD framework (21, 22). The code is publicly available at <https://github.com/dlotfi/MedOODFlow>. All experiments were conducted on a single NVIDIA RTX 6000 GPU.

To evaluate whether our proposed method can effectively detect OOD samples, we utilized a classification model pre-trained on ID data. Our objective is to achieve OOD detection without modifying the weights of the trained classifier and without requiring any specific OOD samples during the training process. The classifier we used is a ResNet18 (42), a standard residual network architecture known for its effectiveness in image classification tasks. The ResNet18 architecture comprises five sequential convolutional blocks, each contributing to progressively higher-level feature extraction. Instead of relying solely on the final block's output, we applied average pooling to the output features from all five stages and then concatenated them to construct a comprehensive feature vector. For the MedOOD benchmark dataset, which includes 3D medical images, we trained a 3D-ResNet18 (43) model on the BraTS 2020 T1 dataset for the task of binary classification. On the other hand, the ResNet18 classifier used for MedMNIST was the official pre-trained model provided by the MedMNIST curators, trained on the OrganAMNIST dataset for the task of multi-class classification with 11 classes. We used the feature vectors extracted from backbone stages to train our normalizing flow model for OOD detection. (**Figure 1**). During the training of the OOD detection model, the weights of the backbone were kept frozen to preserve the learned representations. This approach allows for a post-hoc application of our method, enabling integration with existing pre-trained models without the need for retraining or altering their outputs, which is advantageous in clinical settings where regulatory approvals may restrict modifications to established models.

Supplementary Note 2:

To evaluate the generalizability of our method, we curated a new out-of-distribution (OOD) benchmark dataset named MedOOD from publicly available medical image repositories. An overview of the MedOOD benchmark datasets used in this study is provided in **Table S1**. Listed below are the detailed shifts we used to build the 21 OOD datasets, grouped into five categories:

Transformation Shifts: Here we used different transformation shifts to simulate common imaging artifacts and perturbations that degrade image quality. The perturbations included motion artifacts, which simulate head movements during acquisition, causing blurring of sharp edges by applying random rotations ($\pm 10^\circ$) and translations (± 10 mm). Ghost artifacts replicate regions along axes to emulate periodic motion such as cardiac or respiratory movement. Bias artifacts introduce non-uniform illumination due to magnetic field inhomogeneity, created using a linear combination of polynomial basis functions. Spike artifacts produce periodic stripes (Herringbone artifact) by mimicking RF pulse abnormalities due to aberrant points in k-space. Gaussian noise adds random noise with zero mean and a standard deviation of 0.5 to normalized images. Downsampling simulates low-resolution or anisotropic voxel sizes by downsampling images in random dimensions and interpolating back to the original resolution. Scaling perturbations modify the apparent size of the brain by shrinking it by half or doubling it. Gamma alterations simulate extreme contrast changes by raising intensity values to the powers of $e^{1.5}$ or $e^{-1.5}$. Truncation crops half of the image in a random direction, emulating file transfer errors or missing slices. Erroneous registration introduces noise to the 3D affine registration matrix, emulating alignment errors with the SRI24 atlas. For each of this transformation we made 75 OOD samples (**Figure 2B**)

Population Shifts: Population shifts occur when the test data deviate from the population used for training. These shifts were evaluated using auxiliary datasets from BraTS 2023, including pediatric subjects (44) and patients from Sub-Saharan Africa (45). The pediatric dataset comprises 99 T1w MRIs of children diagnosed with glioblastoma, preprocessed to align with adult templates to minimize size differences. The Sub-Saharan Africa dataset includes 60 T1w MRIs from various centers in Sub-Saharan Africa, typically of lower quality and representing more advanced disease stages due to late diagnosis. Samples of these two datasets are shown in **Figure 2C**.

Modality Shifts: Modality shifts simulate cases where the imaging modality differs from the expected T1w MRI. We included FLAIR and contrast-enhanced T1 (T1ce) sequences corresponding to the 75 ID test subjects from BraTS 2020 (32), representing less drastic and more challenging modality shifts, respectively. Additionally, we incorporated 150 pre-contrast brain CT scans from the CQ500 dataset (46), providing a clear contrast to the expected MRI modality. Illustrated in **Figure 2D**.

Diagnostic Shifts: Diagnostic shifts test the model's ability to handle images containing pathologies unseen during training. We used datasets including 170 T1w MRIs from the WHM 2017 dataset (47) corresponding to patients with multiple sclerosis; 150 T1w MRIs from the ATLAS R2.0 dataset (48) representing patients with stroke; 150 T1w MRIs from the EPISURG dataset (49) of patients who underwent brain resection for epilepsy treatment; and 150 T1w

MRIs of young, healthy adults from the IXI dataset (50). **Figure 2E** shows a few examples from these datasets.

Organ Shifts: Organ shifts represent extreme cases where the input data are entirely unrelated to the brain MRI domain. These datasets include 80 T1w abdominal MRIs from the CHAOS dataset (51) and 150 lumbar spine T1w MRIs from the Lumbar Spine MRI dataset (52). (**Figure 2F**)

Supplementary Note 3:

Ablation study: To further investigate the factors contributing to the superior performance of our proposed normalizing flow-based method, we conducted a comprehensive ablation study examining the impact of three key elements: (1) the number of backbone stages used for feature extraction, (2) the number of training epochs, and (3) the percentage of training data utilized. We analyzed the performance of our method when using features extracted from different numbers of backbone stages. The results demonstrate that utilizing features from all five stages consistently leads to the best performance across all OOD detection metrics (**Figure S2**). This indicates that the inclusion of hierarchical features, ranging from low-level to high-level representations, significantly enhances the model’s ability to discern ID and OOD samples. However, using features from the two last stages yields the best results for diagnostic and population shifts in MedOOD, which shows that higher-level semantic features are particularly effective in capturing certain types of distributional differences.

We explored the effect of training duration by varying the number of training epochs. Among all configurations tested, training the model for 100 epochs yielded the optimal performance, achieving the highest AUROC values (93.8% for MedMNIST and 84.61% for MedOOD). However, training for only 10 epochs achieved 88.44% AUROC on MedMNIST and 83.03% on MedOOD, corresponding to 94% and 98% of the performance at 100 epochs, respectively (**Figure S3**). This demonstrates that the model achieves most of its performance gains early in training, making shorter training durations a highly efficient option. Besides, to evaluate the robustness of our method under limited data settings, we trained the model on varying percentages of the training data (25%, 50%, and 100%). Our method demonstrated strong performance even when trained on only 25% or 50% of the available data, achieving AUROC values of 92.66% on MedMNIST and 82.87% on MedOOD at 50% of the data, compared to 93.8% and 84.61% with full data, respectively (**Figure S4**). This underscores the data efficiency of our approach, which can maintain robust OOD detection performance even under resource-constrained conditions.

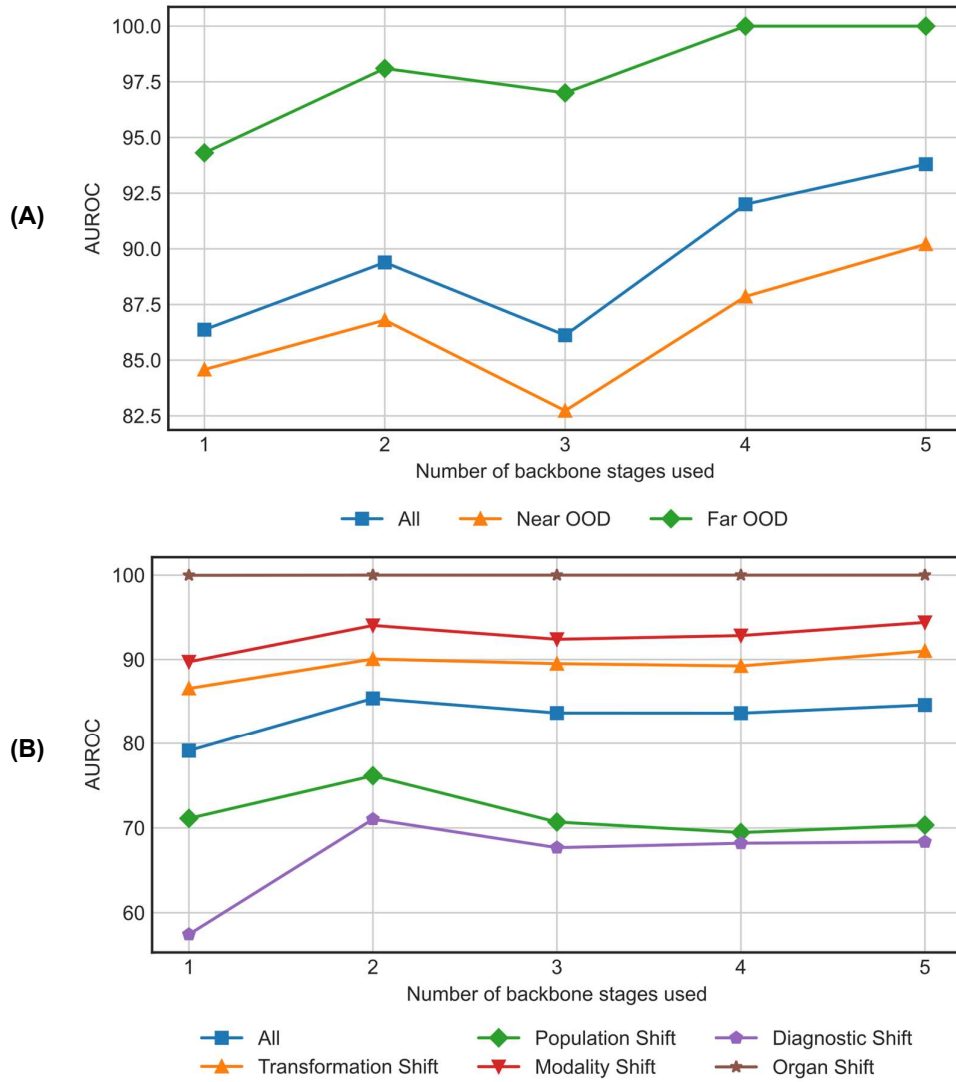


Figure S2: Impact of using features from different number of backbone stages on performance. (A) On MedMNIST (B) On MedOOD

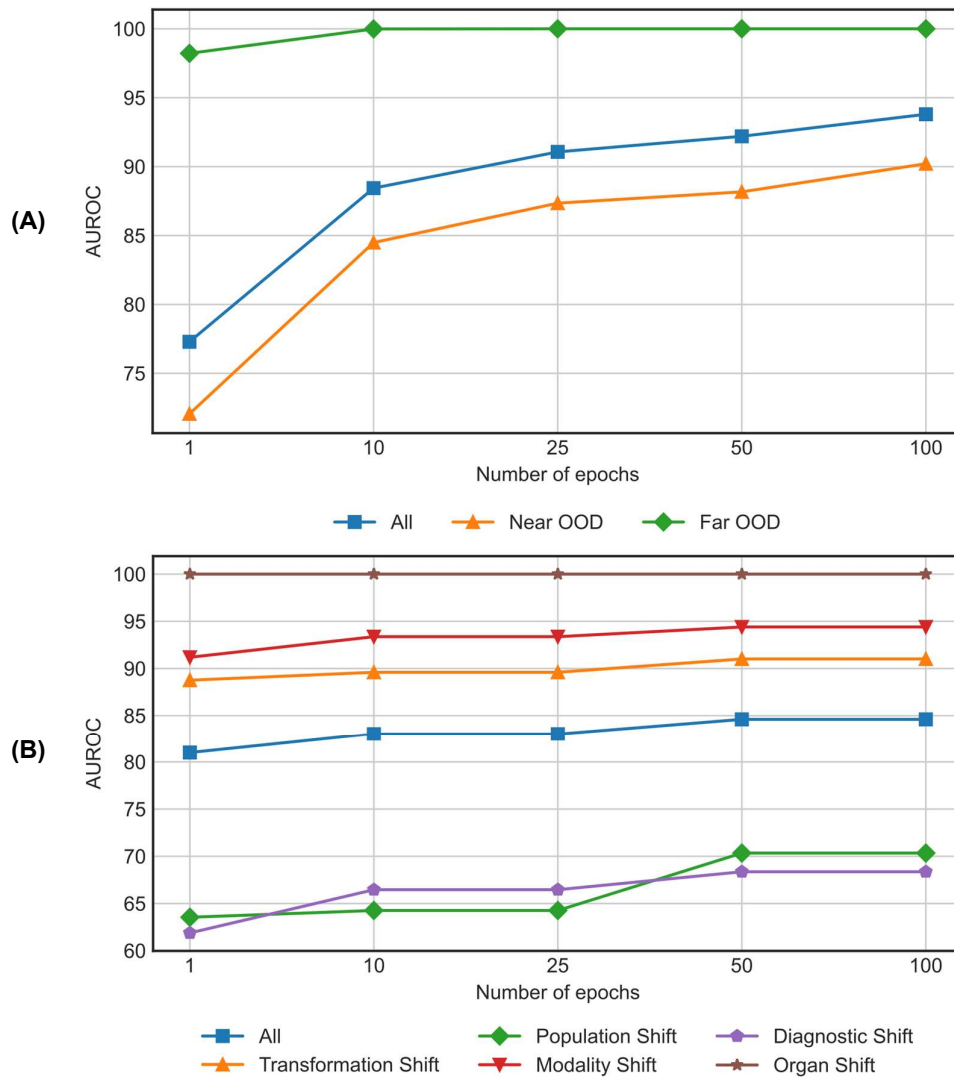


Figure S3: Impact of number of epochs on performance. (A) On MedMNIST (B) On MedOOD

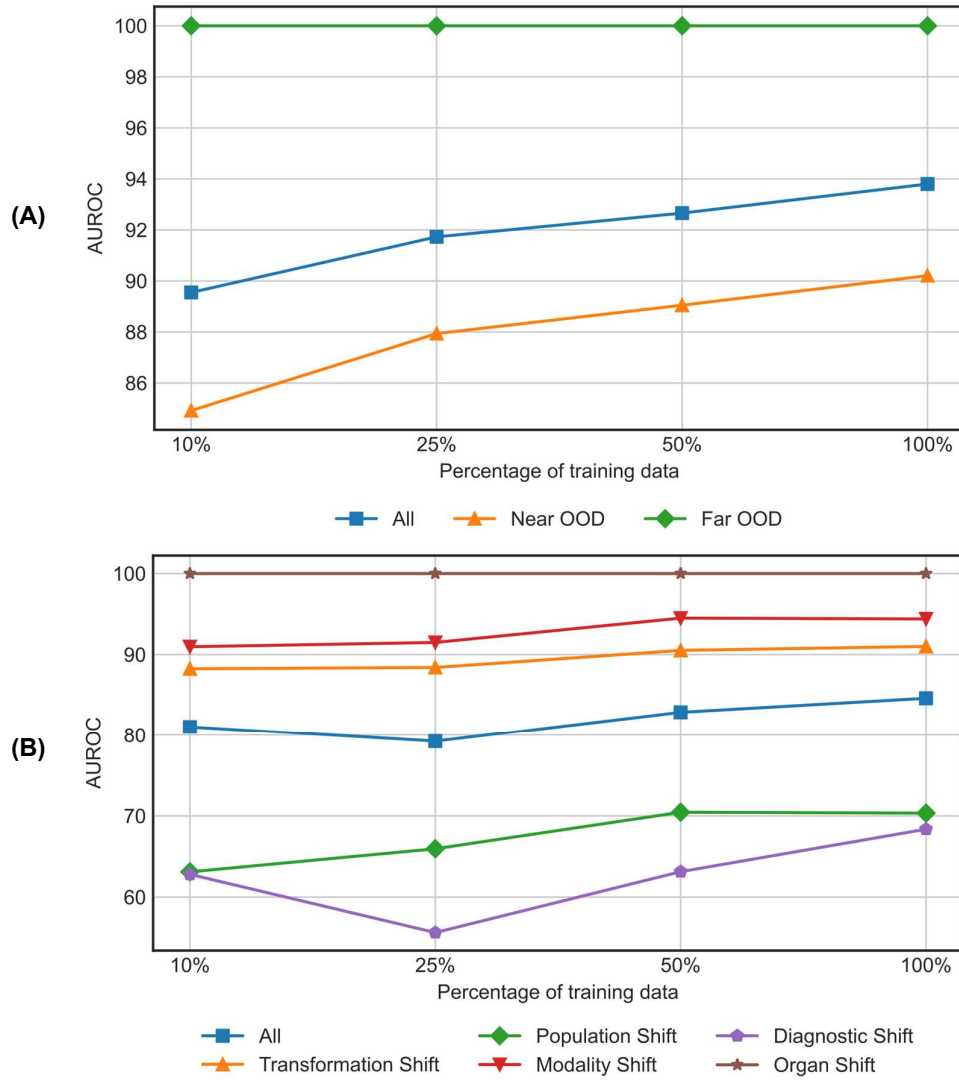


Figure S4: Impact of using different percentage of training data on performance. (A) On MedMNIST (B) On MedOOD